Surface & Coatings Technology 324 (2017) 577–584

Contents lists available at ScienceDirect

Surface & Coatings Technology

journal homepage: www.elsevier.com/locate/surfcoat

Calcium-rich CMAS corrosion induced microstructure development of thermal barrier coatings

Haili Chang [a,b], Canying Cai [a,b,*], Yanguo Wang [a,b], Yichun Zhou [a,b], Li Yang [a,b], Guangwen Zhou [c,**]

[a] School of Materials Science and Engineering, Xiangtan University, Xiangtan 411105, China
[b] Key Laboratory of Low Dimensional Materials & Application Technology of Ministry of Education, Xiangtan University, Xiangtan 411105, China
[c] Department of Mechanical Engineering & Materials Science and Engineering Program, State University of New York, Binghamton, NY 13902, USA

ARTICLE INFO

Article history:
Received 13 April 2017
Revised 25 May 2017
Accepted in revised form 26 May 2017
Available online 26 May 2017

Keywords:
Thermal barrier coatings (TBCs)
CMAS corrosion
Microstructure

ABSTRACT

$Ca_{50}Mg_{10}Al_{10}Si_{30}$ (CMAS) corrosion induced microstructure evolution and composition development in yttria-stabilized zirconia (YSZ) thermal barrier coatings prepared by electron-beam physical vapor deposition (EB-PVD), have been investigated by means of analytical electron microcopy, Raman spectroscopy and X-ray diffraction. The corroded YSZ still mainly consists of t-ZrO_2 and no harmful monoclinic zirconia formation occurs; however, the feathery and columnar morphology of the as-deposited YSZ coating transforms into an equiaxed grain structure with dramatic grain coarsening and significant CMAS infiltration. The CMAS corrosion induces dissolution of YSZ into the molten CMAS, spinel $MgAl_2O_4$ formation both in the intergranular gaps and inside YSZ grains, and anorthite ($CaAl_2Si_2O_8$) precipitates in the intergranular gaps with reduced Mg and Ca content in the infiltrated amorphous CMAS. These results show that CMAS with a high content of calcium can induce significant grain coarsening and microstructure evolution that has a detrimental effect on primary function of the YSZ coating.

1. Introduction

Thermal barrier coatings (TBCs) are key aero-engine materials for protecting the hot components and improving the efficiency [1–4]. TBCs can be prepared by air plasma spraying (APS) or electron beam physical vapor deposition (EB-PVD) [5]. TBCs deposited by EB-PVD have a columnar structure with higher strain tolerance and stronger interfacial bonding strength than those sprayed by APS. Currently, 7 wt% yttria-stabilized zirconia (7YSZ) is a typical TBC material used in gas turbines owing to its high-temperature capability, low thermal conductivity, and the similar thermal expansion match with the superalloy substrate [6].

An important trend in the development of aero-engines is to further improve the thrust weight ratio through higher operating temperature. The most common failure mechanism for TBCs is the detachment of the YSZ coating from the metallic substrate induced by the oxidation of the superalloy. However, a new degeneration and failure mechanism of TBCs has become more prominent with the increase of the in-service temperature [7]. Siliceous mineral debris (dust, sand, and volcanic ash) in air is inevitably ingested by the working turbine engine and deposited on the hot TBC surfaces [8–11]. The debris mainly consists of calcium-magnesium-alumina-silicates (CMAS). The melting point of CMAS depends on its composition. At temperature lower than the melting point, the CMAS debris simply bounces off or cause erosive damage. While at the temperature higher the melting point, CMAS melts and rapidly infiltrates into the YSZ TBCs along pores or gaps in the coatings. After the cooling of the engine, the molten CMAS filled in the pores or the columnar gaps of the YSZ is solidified [8,11–15], which leads to high stress in the coating [16–18]. Meanwhile, the strain tolerance of the YSZ layer decreases and thermal conductivity increases with the filled CMAS. Therefore, the coating with CMAS infiltration is prone to spall and failure due to its weakened thermal insulation performance [8,9,19]. On the other hand, the chemical interaction between molten CMAS and YSZ generates new phases (such as zirconium silicate, calcium feldspar, spinel, etc.) or induces phase transitions in the YSZ coating, leading to significant changes in the morphology, microstructure, and composition of the YSZ coating, even the degradation and failure of the thermal barrier coatings [20,21].

A lot of research works have been performed for investigating the thermal and chemical mechanisms of YSZ corrosion by CMAS. A typical CMAS with the composition of 33CaO–9MgO–13$AlO_{1.5}$–45SiO_2 (in mole percent) was widely used to study the corrosion induced characteristics and mechanism of TBCs [9,14,15,20,22–24], which was based on the average deposits of an aero turbine engine operated in a desert environment as reported by Borom et al. [8], excluding some minor components (Fe and Ni) believed to mainly originate from the engine. CMAS with other compositions has also been applied to investigate

* Correspondence to: C. Cai, School of Materials Science and Engineering, Xiangtan University, Xiangtan 411105, China.
** Corresponding author.
E-mail addresses: cycai@xtu.edu.cn (C. Cai), gzhou@binghamton.edu (G. Zhou).

http://dx.doi.org/10.1016/j.surfcoat.2017.05.076
0257-8972/

CMAS corrosion of TBCs. For example, Mechnich et al. [25] used an artificial ash with less calcium and more silicon (where the content of SiO_2 is close to 60%) to simulate CMAS corrosion of TBCs. Due to the variable CMAS compositions, the thermochemical aspects of the CMAS corrosion induced degradation phenomena may depend on the CMAS composition and further studies are needed to assess their correlation.

The YSZ layer can be rapidly attacked along the grain boundaries via the infiltrated molten CMAS. The YSZ grain growth with calcium diffusion into the YSZ matrix is observed after the chemical reaction reaches equilibrium [10,11]. Previous study mainly focused on the TBC corrosion by CMAS that has less calcium in the composition (the content of CaO < 39.2 mol%) [9,12–15,19–21,25–27]. The main results of these studies are that the CMAS-corroded YSZ layer undergoes the tetragonal to monoclinic phase transition or CMAS reacts with YSZ to generate some new phases such as zirconium silicate, magnesium aluminate spinel, anorthite, etc. Both zirconia and yttrium oxide can dissolve into the glass silicate. When the content of calcium in CMAS is low, zirconia in the glass silicate precedes yttria to reach the solubility limit. Therefore, dissolved zirconia is re-deposited as a fine-grained monoclinic phase, depleted in yttria, in the YSZ layer [10,11]. When the content of calcium in CMAS is high, however, zirconia in the glass silicate does not precede yttria to reach saturation due to the large concentration of modifier atoms (i.e., high CaO contents). Thus, no re-deposition of Y_2O_3-depleted ZrO_2 grains takes place. The microstructure of the residual coating consists of large, round-shaped ceramic grains, consistent with grain-boundary attack followed by grain growth of the ceramic. Diffusion of calcium into the grains also helps to stabilize the tetragonal phase [10,11]. Therefore, the variation in the calcium content in CMAS can lead to a dramatic difference in the degradation behavior of the YSZ coating. However, a deeper analysis of the microstructural feature and the fundamental mechanism for the composition effect on the YSZ corrosion is still lacking. In the present work, we focus on the microstructure characteristic of EB-PVD YSZ TBCs corroded by the Ca-rich CMAS, $Ca_{50}Mg_{10}Al_{10}Si_{30}$, where the Ca content is close to that used by Wet et al. [10,11]. A set of complementary tools including X-ray diffraction (XRD), Raman spectroscopy, scanning electron microscopy (SEM), transmission electron microscopy (TEM) are used to characterize the microstructure and composition feature in CMAS-corroded YSZ.

2. Materials and methods

A 100 μm thick 7 wt% Y_2O_3 partially stabilized ZrO_2 is directly deposited on an alumina (α-alumina, 98% in purity) substrate via an EB-PVD system (UE-204B). This simplified sample structure has two advantages. On the one hand, an alumina as a substrate is capable of enduring higher temperatures than a metallic alloy. On the other hand, the alumina substrate resembles the thermal growth oxide (TGO) formed from the oxidation of an underlying aluminide bond coat for a typical TBC system.

CMAS with the composition of 50CaO-10MgO-10$AlO_{1.5}$-30SiO_2 is prepared for the CMAS corrosion experiment. The preparation process of the CMAS powder is as follows. Firstly, the power of CaO, MgO, Al_2O_3 and SiO_2 is mixed by ball milling; then, the mixture gathered in an corundum crucible is heated in a muffle furnace at 1450 °C for 4 h

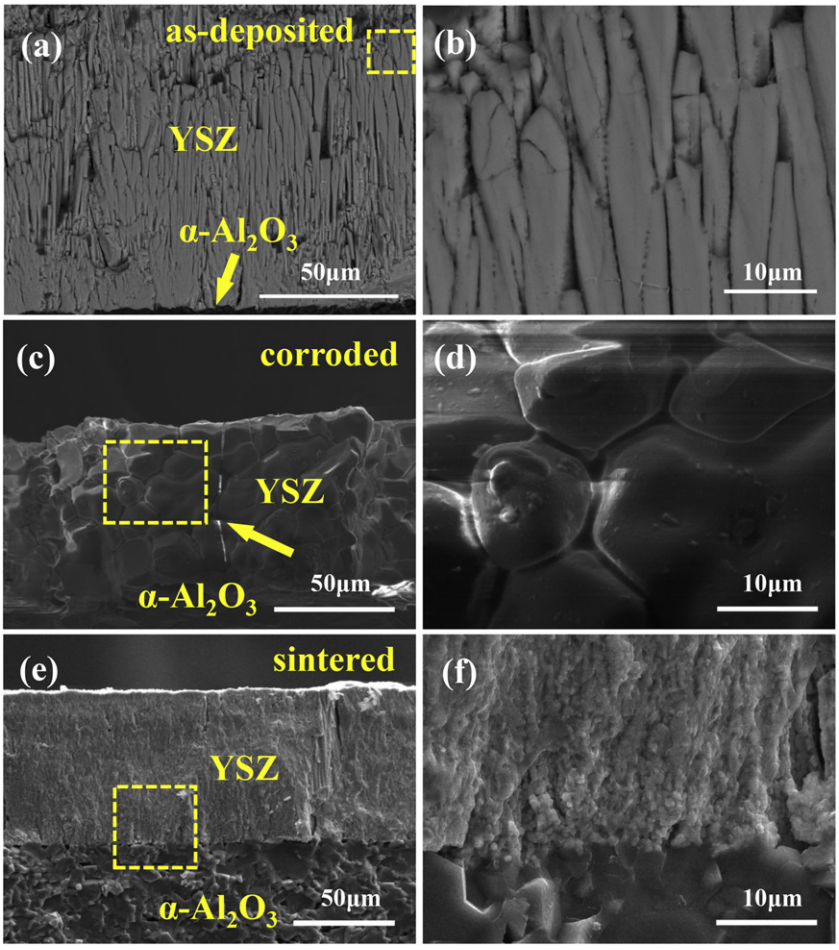

Fig. 1. (a) Cross-sectional SEM morphology image of the as-deposited YSZ; (b) zoomed-in SEM image of the region marked by a dashed yellow square in (a); (c) SEM morphology image of the YSZ coating corroded by molten CMAS at 1400 °C for 4 h; (d) close-up SEM view from the region marked by a dashed yellow square in (c); (e) SEM morphology image of the sample after exposure to 1400 °C for 4 h; (f) zoomed-in SEM image of the YSZ/alumina interface region marked by the yellow square in (e).

in air; after cooling to room temperature, the mixture with the glassy state is manually grinded into fine mortar and pestle; finally, the fine CMAS power is obtained by a Fi500 mesh sieve filter.

The preparation of CMAS-corroded TBC samples is performed as follows. The fine CMAS powder is completely mixed with deionized water and pasted on the as-deposited TBC surface with 10 mg/cm^2 of the CMAS. The CMAS-pasted TBCs are cut into 1 cm × 1 cm pieces and placed in corundum crucibles. The crucibles are kept in a muffle furnace at 1400 °C for 4 h with a heating and cooling rate of 6 °C/min, where the corrosion temperature is set similarly as the work by Wet et al. [10,11]. While Wet et al. [10,11] used very long corrosion time ranging from 20 h–120 h, Krämer et al. [20] found that CMAS fully permeated the TBCs after only 4 h. Therefore, we choose 4 h as the corrosion time in the present study. For comparison, a sintered sample without the CMAS paste is also obtained by performing the same heat treatment as mentioned above.

Raman spectroscopy and XRD are used to identify crystalline phases of the as-deposited coatings and the coatings after the CMAS corrosion. Raman Spectra are obtained using a Renishaw Invia laser Raman Spectrometer. XRD analyses are performed by a D/MAX 2500 diffractometer with Cu Kα radiation. SEM (Qunanta FEG-250, FEI) is used to characterize microstructure, and SEM morphology images are obtained by collecting secondary electrons. Cross-sectional TEM samples are prepared following the conventional process presented in the literature [28]. After dimpling and mechanical polishing using a Gatan dimple grinder (Model: 656), the foils are thinned by Ar ion milling using a PIP system (Model 691, Gatan Inc.). At the initial and final stages of ion milling, the angles of incident Ar + ion beams are set at 15° and 8° and the accelerating voltages are set at 3.8 kV and 2 kV, respectively. The prepared TEM specimens are examined using JEM-2100 TEM.

3. Results and discussion

3.1. SEM characterization

We firstly observe the samples by SEM in order to understand the overall morphology characteristics of the CMAS corroded thermal barrier coatings. Fig. 1 shows representative SEM images of the cross-sectional morphology of the as-prepared sample and the same sample after exposure to 1400 °C for 4 h with or without CMAS. It can be seen that the as-deposited YSZ coating has a thickness of about 120 μm with columnar grains nearly perpendicular to the alumina substrate (Fig. 1(a)). The columnar grains in the upper part are coarse and loose, while those in the bottom part are small and dense. Fig. 1(b) is a zoomed-in SEM image of the region marked by a dashed yellow square in Fig. 1(a), which shows that the columnar grains have an average lateral size of ~300 nm. The staggered columnar grains and the gaps between the columnar grains offer good thermal insulation. Fig. 1(c) is a typical SEM morphology image of the sample corroded by molten CMAS at 1400 °C for 4 h. It can be clearly observed that the columnar grains are completely turned into an equiaxed grain structure with an average grain size of tens of microns. The thickness of the YSZ layer has reduced from the initial ~100 μm to ~70 μm due to the collapse of the original columnar structure. Some white channels as indicated by the yellow arrow in Fig. 1(c) are observed, which may be the charging effect during the SEM imaging due to the poor electric conductivity of the oxide. Fig. 1(d) is a zoomed-in SEM image of the dashed yellow square region in Fig. 1(c), which shows clearly that the original columnar grains have now transformed into equiaxed grains with faceted surfaces. It can be also seen from Fig. 1(c) that the equiaxed grains are not fully coalesced; instead, gaps exist between grains.

In order to further clarify whether the collapse of the columnar structure of the YSZ coating shown above is caused by the high temperature sintering or by CMAS corrosion at the high temperature, a sintered sample without CMAS is obtained under the same heat treatment condition as the CMAS corroded sample shown above. Fig. 1(e) is a representative SEM image of the cross-section morphology of the sintered sample, which shows that the ceramic layer still keeps about the same thickness of ~100 μm as the as-deposited YSZ coating. The columnar crystals become coalescent and the obvious columnar characteristics disappear after the high temperature sintering. Fig. 1(f) is a zoomed-in SEM image of the region marked by a dashed yellow square in Fig. 1(e), which shows that intercolumnar gaps have largely disappeared. Although the overall columnar morphology can still be visible from Fig. 1(e), it can be seen that the initial columnar grains have transformed to smaller and highly coalesced grains with an average lateral size of ~100 nm. The comparison between the two samples with and without the CMAS paste demonstrates that the columnar to equiaxed transition with the significant grain coarsening shown in Fig. 1(c, d) is related to the CMAS corrosion induced thermal and chemical effects, rather than the high temperature effect only.

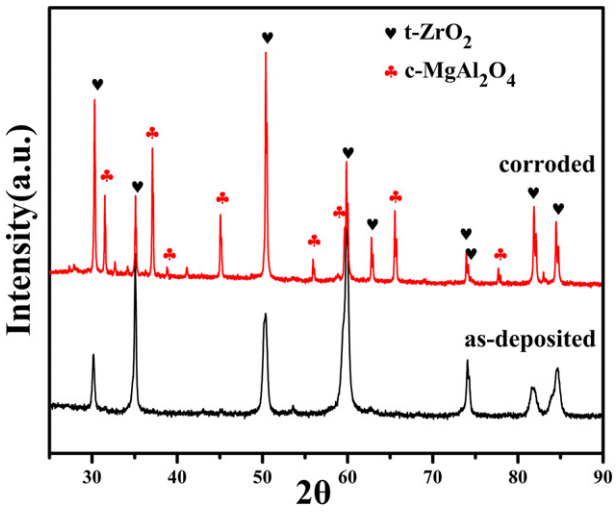

Fig. 2. XRD patterns of the as-deposited YSZ sample, the sample after CMAS corrosion at 1400 °C for 4 h.

3.2. XRD and Raman spectroscopy characterization

In order to identify if any phase transition has happened in the ceramic layers after CMAS corrosion, the samples are examined by XRD

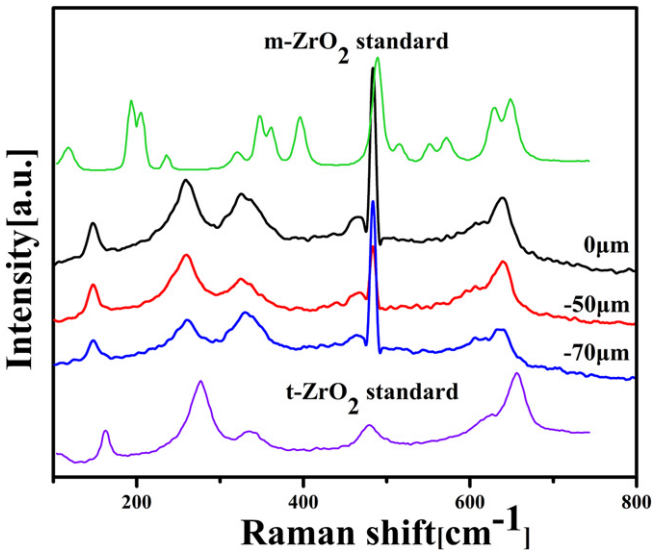

Fig. 3. Raman Spectra of the sample corroded by molten CMAS, where the spectra are taken from the top ceramic layer (YSZ), the middle ceramic layer in the regions about 50 μm down from the surface and the YSZ/Al_2O_3 interface, respectively; and the standard Raman Spectra of m-ZrO_2 is also included for comparison.

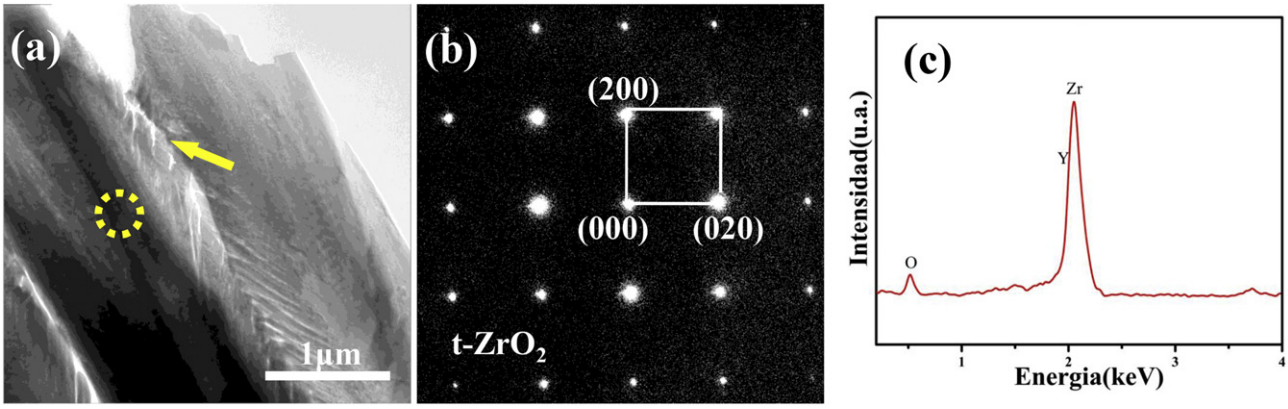

Fig. 4. (a) Bright field TEM image of the as-deposited sample with the "feathery morphology" in the edge region of columnar grains; (b) is a selected area electron diffraction (SAED) pattern taken from the marked red square region; (c) is the energy dispersive spectrum (EDS) analysis of the YSZ layer.

and Raman spectra. The XRD patterns in Fig. 2 are taken from the surface of two samples, i.e., the as-deposited YSZ, the YSZ coating with a CMAS paste annealed at 1400 °C for 4 h. It shows that the as-deposited sample has the tetragonal zirconia structure at room temperature (t-ZrO_2) due to the stabilizing effect of Y_2O_3. The YSZ sample with CMAS corrosion mainly consists of tetragonal zirconia with the extensive presence of a spinel phase ($MgAl_2O_4$). In order to identify if there exists m-ZrO_2 in the corroded sample, the samples are further characterized by Raman spectroscopy that is more sensitive than XRD for detecting m-ZrO_2. Fig. 3 shows the depth-resolved Raman spectra obtained from the CMAS-corroded sample at the surface of the coating (depth ≈ 0 μm), the middle of the coating (depth ≈ 50 μm) and the YSZ/Al_2O_3 interface region (i.e., ≈70 μm below the surface), respectively. For comparison, the standard spectra of m-ZrO_2 and t-ZrO_2 are also included in Fig. 3. It can be seen that the corroded sample shows some typical Raman peaks of t-ZrO_2 at 148 cm^{-1} and 260 cm^{-1}, and there is no presence of the characteristic peaks of m-ZrO_2 at 181 cm^{-1} and 192 cm^{-1}. Therefore, it can be concluded that there is only t-ZrO_2 in the corroded sample, and no phase transition from the tetragonal phase to the monoclinic phase occurs in the YSZ layer from the CMAS corrosion.

3.3. TEM characterization

In order to further reveal the microstructure characteristic of the coatings, the as-deposited and corroded samples are examined by TEM. Fig. 4(a) displays a representative bright-field (BF) TEM image of the as-deposited YSZ coating. The columnar grains of the as-deposited coating show the typical "feathery morphology" along the edges of the grains. Gaps as marked by a yellow arrow are visible along the edges of the columnar grains, where the molten CMAS is prone to penetrate into the coating. Fig. 4(b) is a selected-area electron diffraction (SAED) pattern taken from the area marked by the yellow circle in Fig. 4(a), which can be well-indexed with the t-ZrO_2 structure. The energy dispersive spectrum (EDS) analysis of the YSZ layer indicates that the YSZ consists of elements of Zr, Y and O, as shown in Fig. 4(c). Combining the SAED and EDS analyses, it is confirmed that the YSZ layer has the tetragonal phase (in which Y is distributed randomly), which is consistent with the XRD diffraction and Raman analyses.

The top (close to the CMAS paste), middle and bottom (close to the YSZ/Al_2O_3 interface) sections of the CMAS-corroded YSZ are carefully examined by TEM. Fig. 5(a) shows a typical BF TEM image from the middle section of the corroded YSZ. It can be seen from the TEM image that the CMAS corrosion results in the formation of micron-sized particles with faceted or round surfaces and the presence of gaps between grains, consistent with the SEM observation as shown in Fig. 1(d). Further TEM analysis shows that the gaps in the grain boundaries are filled with other material that shows bright TEM image contrast. EDS analysis shows that the spherical particle with the dark contrast consists of elements of Zr, Y and O, there is also a small amount of copper, as shown in Fig. 5(b), indicating that it is also zirconia as the same as Fig. 4. Inserted in the left bottom of Fig. 5(a) is a SAED pattern taken from the gap area as marked by a yellow solid arrow in Fig. 5(a). The diffuse diffraction rings indicate that the material filled in the gaps between particles has an amorphous state. EDS analysis of the area indicated by the yellow solid arrow region in Fig. 5(a) shows the presence of Al, Si and Ca in addition to the peaks of O, Zr, Y and Cu, as shown in Fig. 5(c). The Cu peak

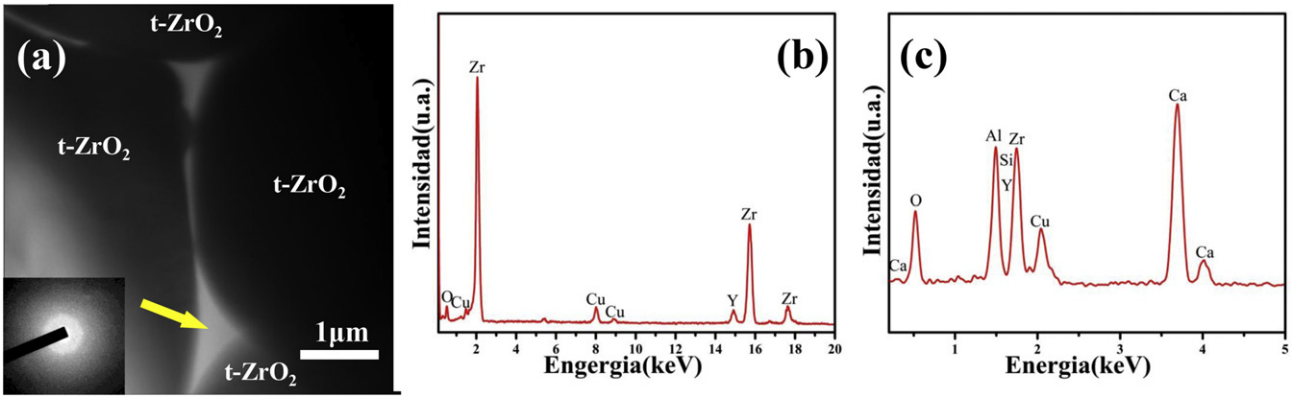

Fig. 5. (a) BF TEM image from the YSZ coating corroded with CMAS for 4 h; Inserted in the left bottom of Fig. 5(a) is a SAED pattern taken from the infiltrated CMAS in the intergranular gap (marked by the yellow arrow); (b) EDS analysis of the spherical particle with the dark contrast consists, where the Cu signal is an artifact from the TEM grid; (c) EDS composition analysis of the infiltrated CMAS shown in (a).

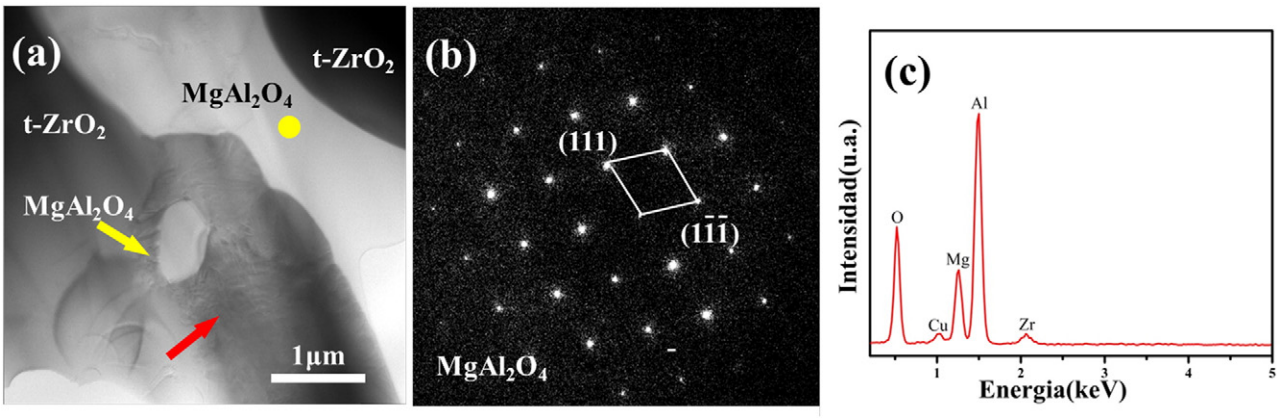

Fig. 6. (a) BF TEM image from another typical area in the middle section of the corroded YSZ coating; (b) SAED analysis on white filler (marked with a solid yellow dot in (a)); (c) EDS composition analysis on the white filler.

in the EDS profile stems from the TEM Cu support. It is worth mentioning that the as-prepared CMAS contains 10 at.% Mg. The absence of Mg signals in the EDS indicates that the molten CMAS has undergone composition segregation, which can be driven by the formation of the spinel $MgAl_2O_4$ that results in the depletion of Mg from the amorphous deposition in the intercolumnar gaps. The presence of strong Zr signal in the EDS profile shows that Zr has been dissolved in the molten CMAS.

Fig. 6(a) shows a BF TEM image from another typical area in the middle section of the corroded YSZ coating. EDS and SAED analyses indicate that the areas with the relatively darker contrast are t-ZrO_2, which is similar to Fig. 5. The gaps between the t-ZrO_2 grains are full of depositions with the much brighter contrast. To identify the nature of the deposition, the area marked by a solid yellow dot in Fig. 6(a) is analyzed by EDS and SAED. EDS analysis shows that the main elements in the area are O, Mg and Al, as shown in Fig. 6(c). The SAED pattern from the deposit in the intercolumnar gap can be well-indexed with the $MgAl_2O_4$ structure, as shown in Fig. 6(b). A polygonal precipitate as indicated by the yellow arrow shown in Fig. 6(a) is formed in the interior of the t-ZrO_2 grain and the precipitate shows the similar bright contrast as the deposit in the intercolumnar gap. EDS and SAED analyses show that the precipitate is also $MgAl_2O_4$. The observed $MgAl_2O_4$ particle inside the t-ZrO_2 grain indicates that the molten CMAS can filtrate through the YSZ lattice and precipitate as the crystalline spine phase. This process requires etching the t-ZrO_2 grain in order to accommodate the volume for the $MgAl_2O_4$ precipitate.

It can be seen from Fig. 6(a) that the t-ZrO_2 grain area that surrounds the $MgAl_2O_4$ precipitate shows the contrast of stripe fringes. Fig. 7(a) is a zoomed-in TEM image from the t-ZrO_2 grain area indicated by a red arrow as show in Fig. 6(a), which shows clearly the stripe fringe contrast. The EDS analysis shows that this area is dominated by O, Zr, and Y, as shown in Fig. 7(c). Fig. 7(b) is a SAED pattern obtained from the area shown in Fig. 7(a), which shows superlattice spots in addition to the fundamental diffraction spots associated with the t-ZrO_2 phase. The presence of the superlattice spots can be contributed to the ordering of Y atoms in the t-ZrO_2 lattice. The diffraction can be indexed with the $L1_0$-like cation-ordered $Y_{0.5}Zr_{0.5}O_{2-x}$ structure [29,30], in which the Y content is increased significantly from the original doping level of 3.7 mol% Y_2O_3 to 50 mol%. The $MgAl_2O_4$ precipitate induced formation of the cation-ordered phase with the significant Y enrichment in the surrounding area of the YSZ grain suggests that Zr atoms in the YSZ grain are preferentially etched by the molten CMAS, leaving behind a large number of Y atoms that self order in the surrounding area of the remaining YSZ grain.

Fig. 8(a) is a BF TEM image obtained from the top section of the corroded YSZ coating. In the center area is a large inter-grain gap formed with spherical zirconia particles that show much darker contrast. Fig. 8(b) is a SAED pattern from the center area with the bright contrast shown in Fig. 8(a), which can be indexed well with anorthite ($CaAl_2Si_2O_8$). Fig. 8(c) is an EDS spectrum obtained from the gap area as marked by the yellow triangle in Fig. 8(a), which shows the presence of O, Al, Si and Ca. Quantification of the EDS measurements gives the atomic composition of 14.91 mol% Ca, 28.94 mol% Al, 23.12 mol% Si, which is close to the composition of the anorthite phase. In addition, some anorthite is also found at the bottom of the YSZ coatings. XRD does not detect anorthite, which maybe owe to its too little amount.

Fig. 9(a) is a TEM BF image obtained from the bottom section (close to the YSZ/alumina interface) of the corroded YSZ coating. It can be seen that significant $MgAl_2O_4$ develops at the interface region. Meanwhile,

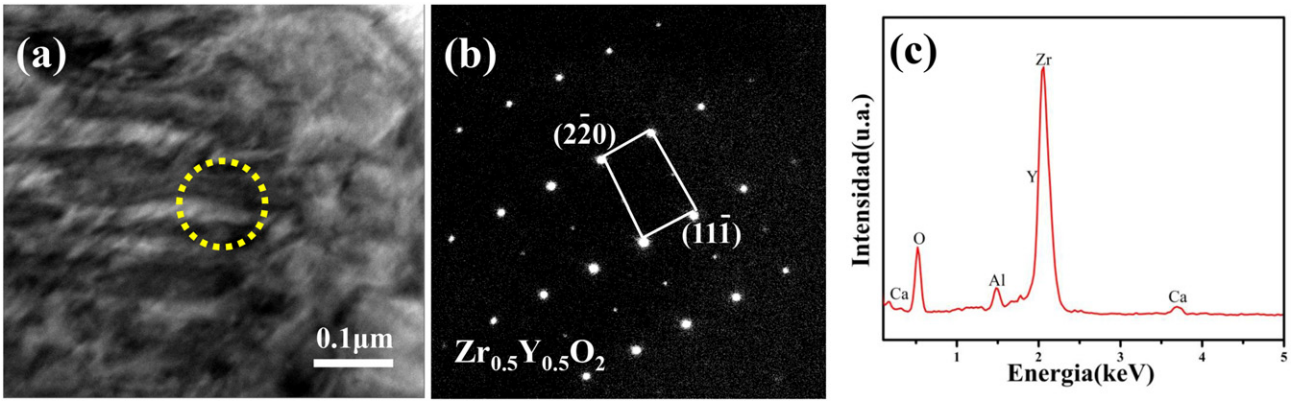

Fig. 7. Enlarged TEM view of the stripe morphology of the YSZ region indicated with a red arrow as shown in Fig. 6(a); (b) SAED pattern from the region marked by the yellow circle shown in (a); (c) EDS composition analysis of the striped region in (a).

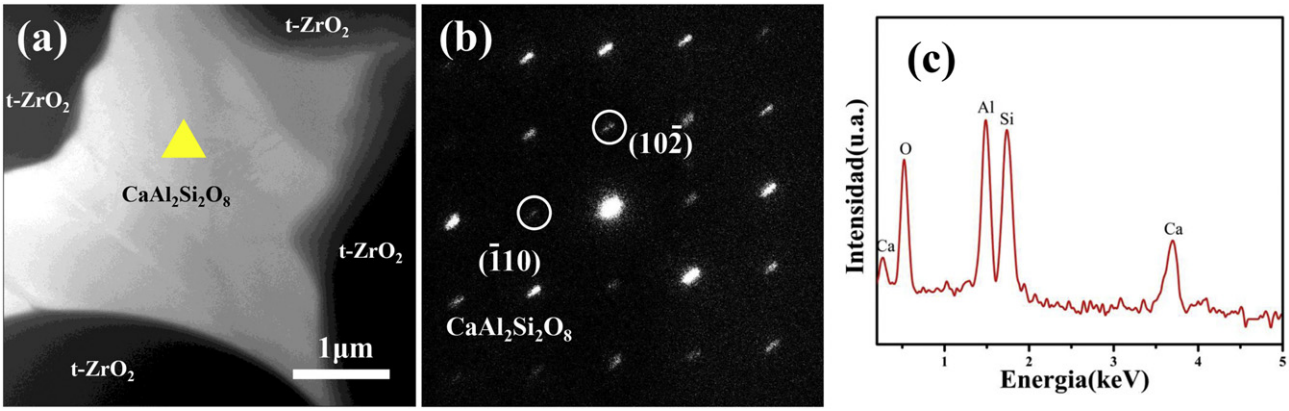

Fig. 8. (a) BF TEM image from the top section of the YSZ layer after the CMAS corrosion at 1400 °C for 4 h; (b) SAED pattern from the center area with the bright contrast in (a); (c) EDS spectrum obtained from the gap area as marked by the yellow triangle in (a).

the YSZ layer is disintegrated into smaller particles with the significant presence of α-Al_2O_3 between t-ZrO_2 grains. Fig. 9(b) is an EDS spectrum from the alumina area marked by the yellow triangle in Fig. 9(a), which shows the minor presence of Ca and Si in the alumina particle.

In addition, we also analyze the composition of the top, middle, and bottom sections of the YSZ coating using EDS in TEM. Table 1 lists the EDS measured compositions averaged over the different locations of each section. Through the EDS analysis of the corroded YSZ, we can find that the upper layer of the corroded YSZ consists of mainly Zr and Y, with the Y/Zr atomic ratio of 0.075, which is slightly lower than the as-prepared coating (0.087). Minor amount of Ca (2.21 mol%) and Al (3.07 mol%) is also present in the top layer. The main composition of the CMAS filled in the intergranular gaps in the top layer is 21.18CaO-0.62MgO-21.71$AlO_{1.5}$-18.37SiO_2 (mole percent), in which the Al content has increased while the other contents have decreased compared to the composition of the original CMAS. Meanwhile, a small amount of Zr (6.18 mol%) and Y (1.75 mol%) has also dissolved in the molten CMAS in the intergranular gap.

The YSZ in the middle layer is still t-phase zirconia with the composition of 63.23 mol% ZrO_2, 6.2 mol% $YO_{1.5}$ and the Y/Zr atomic ratio of 0.098, which is slightly high than the as-prepared YSZ. In addition, 2.54 mol% Ca, 5.32 mol% Al element are also found in the YSZ grain. The main component of the CMAS filled in the intergranular gap in the middle layer is 26.41CaO-24.47$AlO_{1.5}$-20.28SiO_2 with the absence of Mg and slightly increased Al compared to the original composition of the as-prepared CMAS. In addition, 16.18 mol% Zr, and 2.61 mol% Y element are dissolved in the molten CMAS in the middle layer.

The YSZ grains in the bottom layer of the corroded coating are still t-phase zirconia with the composition of 61.147 mol% ZrO_2, 7.04 mol% $YO_{1.5}$ and the increased Y/Zr atomic ratio of 0.114 compared to the as-prepared YSZ. In addition, 2.95 mol% Ca, 7.97 mol% Al element are also found in the YSZ grains, suggesting the diffusion of minor amount of Ca and Al into the YSZ grains. The main components of the CMAS filled in the intergranular gaps in the bottom layer is 12.83CaO-23.42$AlO_{1.5}$-16.97SiO_2, in which the Al content has increased while the other contents have decreased compared to the as-prepared CMAS. Meanwhile, a small amount of Zr is found in the molten CMAS but Y is absent.

4. Discussion

As shown above, the morphology of the YSZ coating has undergone dramatic changes induced by the $Ca_{50}Mg_{10}Al_{10}Si_{30}$ corrosion. The original columnar crystal structure is completely transformed into an equiaxed grain structure with significant grain coarsening although the t-phase zirconia is still maintained. Between the YSZ particles are filled with amorphous CMAS, anorthite, and magnesium aluminum spinel. Meanwhile, magnesium aluminum spinel can also precipitate inside zirconia particles, indicating the significant diffusion of Mg and Al into the YSZ lattice and then precipitating as $MgAl_2O_4$ particles as reaching their saturated solubility in the YSZ lattice. Comparing with the sintered samples (without the CMAS paste), we can find that the collapse of the columnar structure of the YSZ coating is caused by CMAS corrosion, which in turn significantly reduces the primary function (i.e., thermal barrier) of the coating.

Through the composition analysis of the corroded coating (Table 1), we find that the Y/Zr atomic ratio in the YSZ grains is kept nearly the original one. This can be attributed to the limited solubility of other elements (e.g., Ca, Al, Si) in the YSZ lattice, for which the Ca and Al in the

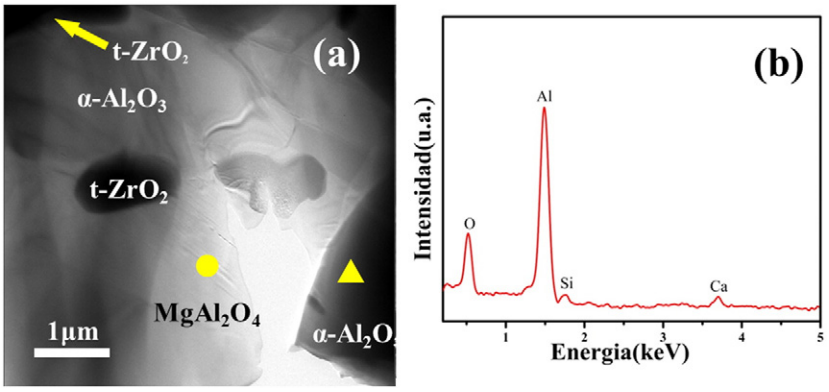

Fig. 9. (a) BF TEM image obtained from the bottom section (close to the YSZ/alumina interface) of the corroded YSZ coating; (b) EDS spectrum from the alumina area marked by the yellow triangle in (a).

Table 1
Compositions measured by EDS point analysis averaged over the different locations in each section of the CMAS corroded YSZ coating. For comparison, compositions of the as-prepared YSZ and CMAS are also given.

Region	Constituent (mol%)	Ca	Mg	Al	Si	Zr	Y
As-deposited	Zirconia					92	8
Top layer of YSZ	Zirconia	2.21	0	3.07	0	74.73	5.58
Middle layer of YSZ	Zirconia	2.54	0	5.32	0.23	63.23	6.2
YSZ/Al_2O_3 interface	Zirconia	2.95	0	7.97	0	61.147	7.04
Original	CMAS	50	10	10	30		
Top layer of YSZ	CMAS	21.18	0.62	21.71	18.37	6.18	1.75
Middle layer of YSZ	CMAS	26.41	0	24.47	20.28	16.18	2.61
YSZ/Al_2O_3 interface	CMAS	12.83	0	23.42	16.97	1.5	0

YSZ lattice can easily precipitate as $MgAl_2O_4$ particles. $MgAl_2O_4$ precipitates are found in the YSZ grains through the entire YSZ layer, indicating the filtration of the CMAS molten into the whole YSZ coating. From the upper part of the ceramic layer to the bottom layer near the YSZ/alumina interface, the content of calcium is increased slightly, while the increase in aluminum is more obvious, as shown in Table 1.

We can find from Table 1 that the content of Ca in the infiltrated CMAS decreases from the upper part of the ceramic layer to the YSZ/alumina interface region. Mg is barely detectable in the CMAS filled in the intergranular gaps, suggesting that Mg preferentially diffuses into the YSZ lattice and then forms $MgAl_2O_4$ precipitates. There is no significance difference in the content of Al in the infiltrated CMAS through the entire coating, but the Al composition is higher than that in the as-prepared CMAS, indicating the outward diffusion of Al from the alumina substrate. The Si content has no significant difference through the entire YSZ coating, remaining at about 18 mol%, which is slightly lower that in the as-prepared CMAS paste. In addition, in the upper and middle sections of the corroded YSZ coating, a small amount of Y and Zr has dissolved in the amorphous CMAS in the intergranular gaps. At the bottom layer near to the YSZ/alumina interface, the accumulation of molten CAMS results in the disintegration of the YSZ grains into tiny YSZ particles surrounded by the amorphous CMAS deposit.

Schematic illustrations of the microstructure feature of the as-deposited YSZ and the YSZ corroded with CMAS at 1400 °C for 4 h are displayed in Fig. 10(a, b), respectively. As shown in Fig. 10(a), the as-prepared EB-PVD YSZ coating has a columnar grain structure with aligned intercolumnar gaps. During the CMAS corrosion, the intercolumnar gaps are the main infiltration channels of the molten CMAS. In addition, the molten CMAS (mostly, Mg and Al atoms) can also penetrate into the YSZ grains, which results in $CaAl_2Si_2O_8$ and $MgAl_2O_4$ precipitation thereby inducing the disintegration of the YSZ grains. As shown in Fig. 10(b), the thickness of the ceramic layer after the CMAS corrosion decreases from 100 μm to about 70 μm. The YSZ coating morphology has changed from the original columnar grain structure into an equiaxed grain structure with significant grain growth. $CaAl_2Si_2O_8$ can only formed in the intergranular gaps, while $MgAl_2O_4$ can form both inside YSZ grains and at intergranular gaps, particularly populated in the bottom section near to the YSZ/alumina interface.

Combined with the composition analysis shown in Table 1, it can be found that the Ca content in the infiltrated amorphous CMAS is lower than that in the as-prepared CMAS. This is due to the thermochemical reaction of the CMAS with the YSZ that produces $CaAl_2Si_2O_8$, which consumes a significant amount of Ca and Si. This also explains why the Si content in the infiltrated amorphous CMAS is lower than the as-prepared CMAS. The formation of a large amount of $MgAl_2O_4$ in the middle and bottom sections of the corroded coating requires the consumption of a lot of Mg and Al, which results in the depletion of Mg in the infiltrated amorphous CMAS, while the alumina substrate provides additional Al through the outward diffusion for $MgAl_2O_4$ growth.

The CMAS attack can result in the dissolution of both yttria and zirconia in the molten CMAS. The solubility of yttria and zirconia in the molten CMAS depends on the CaO content. For CMAS with a low content of CaO, the solubility limit of zirconia is reached before yttria, which results in the precipitation of yttria-depleted ZrO_2 grains in the molten CMAS. The depletion in yttria induces the destabilization of tetragonal phase and monoclinic transformation upon cooling [10–11].

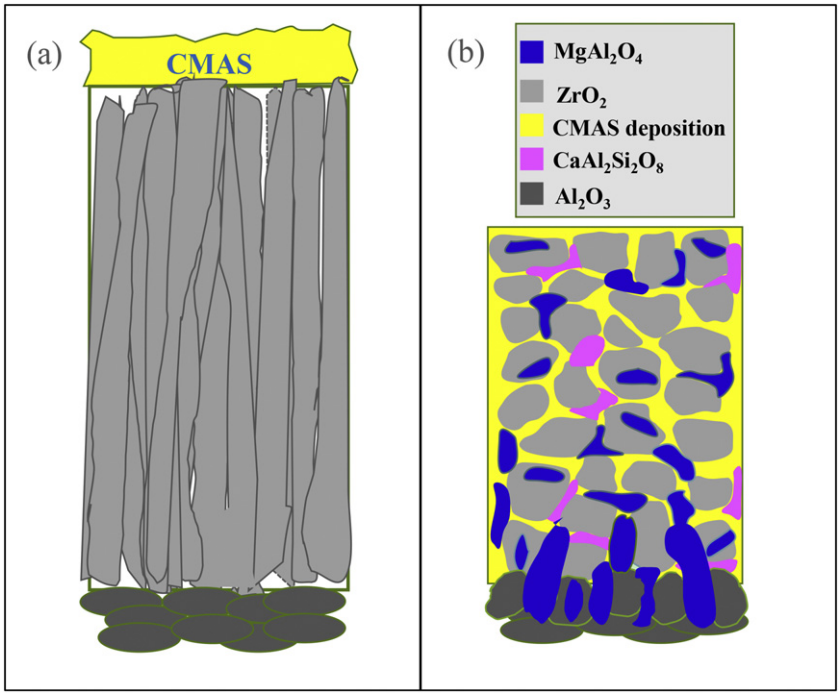

Fig. 10. Schematic illustrations showing the CMAS-corrosion induced microstructure degradation in the YSZ coating; (a) as-deposited YSZ coating with the columnar grain structure; (b) the YSZ coating corroded with CMAS at 1400 °C for 4 h.

By contrast, CaO-rich CMAS shows large solubility for both yttria and zirconia, for which no precipitation of yttria-depleted ZrO_2 grains takes place. This is consistent with the composition measurements shown in Table 1, which show that the yttria content in remaining YSZ is still close to the as-prepared YSZ. Although there is no harmful tetrahedral → monoclinic phase transformation in zirconia during its reaction with the CaO-rich CMAS, the formation of $MgAl_2O_4$ and $CaAl_2Si_2O_8$ precipitates can induce significant growth stress in the YSZ coating and at the YSZ/alumina interface because of the significantly larger lattice constants of $MgAl_2O_4$ spinel (a = b = c = 8.0831 Å, $\alpha=\beta=\gamma=90^\circ$) and the anorthite (a = 8.1768 Å, b = 12.8768 Å, c = 7.0845 Å, $\alpha=93.17^\circ$, $\beta=115.85^\circ$, $\gamma=91.22^\circ$) than those of the zirconia and alumina. These growth stresses can damage the integrity of the YSZ coating and induce delamination at the YSZ/alumina interface. Besides, the thermal expansion coefficients of $CaAl_2Si_2O_8$ (5.0 ppm/°C) and $MgAl_2O_4$ spinel (7.6 ppm/°C) are smaller than those of zirconia (11.0 ppm/°C) and alumina (8.0 ppm/°C). In the cooling process, their thermal expansion mismatch leads to the generation of thermal stress, which also can induce damage to the coating.

5. Conclusion

EB-PVD YSZ TBCs corroded by synthetic CMAS with the composition of 50CaO-10MgO-10$AlO_{1.5}$-30SiO_2 (in molar percentage) at 1400 °C in air for 4 h have been investigated in detail. It is shown that the CMAS corrosion transforms the feathery and columnar morphology of the as-deposited YSZ coating into an equiaxed grain structure with dramatic grain coarsening and significant infiltration of molten CMAS into the intergranular gaps, which can significantly reduce the primary function of the thermal barrier coating. It is found that the corroded YSZ still mainly consists of t-ZrO_2 and no harmful monoclinic zirconia formation occurs since the yttria content in the remaining YSZ grains remains close to the as-prepared YSZ. However, the ordering of locally enriched Y results in the formation of a superstructure of $Y_{0.5}Zr_{0.5}O_{2-x}$ in small areas of YSZ grains. The reaction between CMAS and YSZ ceramic layer generates spinel $MgAl_2O_4$ both in the intergranular gaps and inside YSZ grains with the depletion of Mg in the infiltrated amorphous CMAS and the diffusion of additional Al from the alumina substrate to ceramic coating. Meanwhile, the formation of $MgAl_2O_4$ precipitates inside the YSZ grains is accompanied with the dissolution of YSZ into the molten CMAS. The microstructure analyses also show the formation of $CaAl_2Si_2O_8$, mainly in the intergranular gaps of the corroded coating, resulting in reduced Ca content in the infiltrated amorphous CMAS.

Acknowledgments

This work was supported by the National Natural Science Foundation of China (grant nos. 51590891, 51672233 and 11672256), the opening project of State Key Laboratory of Explosion Science and Technology (Beijing Institute of Technology, the opening project No. KFJJ15-05M) and “Hundred Talents Program” of Hunan Province, China.

References

[1] N.P. Padture, M. Gell, E.H. Jordan, Materials science—thermal barrier coatings for gas-turbine engine applications, Science 296 (2002) 280–284.
[2] R.A. Miller, Thermal barrier coatings for aircraft engines: history and directions, J. Therm. Spray Technol. 6 (1) (1997) 35–42.
[3] U. Schulz, C. Leyens, K. Fritscher, M. Peters, B. Saruhan-Brings, O. Lavigne, J.M. Dorvaux, M. Poulain, R. Mevrel, M.L. Caliez, Some recent trends in research and technology of advanced thermal barrier coatings, Aerosp. Sci. Technol. 7 (2003) 73–80.
[4] R.A. Miller, Current status of thermal barrier coatings—an overview, Surf. Coat. Technol. 30 (1987) 1–11.
[5] B. Gleeson, Thermal barrier coatings for aeroengine applications, J. Propuls. Power 22 (2) (2006) 375–383.
[6] M.J. Stiger, N.M. Yanar, M.G. Topping, F.S. Pettit, G.H. Meier, Thermal barrier coatings for the 21st century, Z. Metallkd. 90 (12) (1999) 1069–1078.
[7] Y.C. Zhou, Q.X. Liu, L. Yang, D.J. Wu, W.G. Mao, Failure mechanisms and life prediction of thermal barrier coatings, Guti Lixue Xuebao/Acta Mech. Solida Sin. 31 (5) (2010) 504–531.
[8] M.P. Borom, C.A. Johnson, L.A. Peluso, Role of environment deposits and operating surface temperature in spallation of air plasma sprayed thermal barrier coatings, Surf. Coat. Technol. 86-87 (1996) 116–126.
[9] P. Mohan, T. Patterson, B. Yao, Y. Sohn, Degradation of thermal barrier coatings by fuel impurities and CMAS: thermochemical interactions and mitigation approaches, J. Therm. Spray Technol. 19 (1–2) (2010) 156–167.
[10] D.J. De Wet, R. Taylor, F.H. Stott, Corrosion mechanisms of ZrO_2-Y_2O_3 thermal barrier coatings in the presence of molten middle-east sand, J. Phys. IV Colloque 3 (C9) (1993) 655–663.
[11] F.H. Stott, D.J. De Wet, R. Taylor, Degradation of thermal-barrier coatings at very high-temperatures, MRS Bull. 19 (10) (1994) 46–49.
[12] J. Wu, H.B. G, Y.Z. G, S.K. G, Microstructure and thermo-physical properties of yttria stabilized zirconia coatings with CMAS deposits, J. Eur. Ceram. Soc. 31 (10) (2011) 1881–1888.
[13] C.Y. Cai, S. Chang, Microstructure characteristics of EB-PVD YSZ thermal barrier coatings corroded by molten volcanic ash, Surf. Coat. Technol. 286 (2016) 49–56.
[14] S. Krämer, J. Yang, C.G. Levi, C.A. Johnson, Thermochemical interaction of thermal barrier coatings with molten CaO-MgO-Al_2O_3-SiO_2 (CMAS) deposits, J. Am. Ceram. Soc. 89 (10) (2006) 3167–3175.
[15] K.M. Grant, S. Krämer, G.G.E. Seward, C.G. Levi, Calcium–magnesium alumino-silicate interaction with yttrium monosilicate environmental barrier coatings[J], J. Am. Ceram. Soc. 93 (10) (2010) 3504–3511.
[16] X. Chen, Calcium–magnesium–alumina–silicate (CMAS) delamination mechanisms in EB-PVD thermal barrier coatings, Surf. Coat. Technol. 200 (2006) 3418.
[17] X. Chen, M.Y. He, I. Spitsberg, N.A. Fleck, J.W. Hutchinson, A.G. Evans, Mechanisms governing the high temperature erosion of thermal barrier coatings, Wear 256 (7–8) (2004) 735–746.
[18] C. Mercer, S. Faulhaber, A.G. Evans, R. Darolia, A delamination mechanism for thermal barrier coatings subject to calcium-magnesium-alumino-silicate (CMAS) infiltration, Acta Mater. 53 (4) (2005) 1029–1039.
[19] R. Wellman, G. Whitman, J.R. Nicholls, CMAS corrosion of EB-PVD TBCs: identifying the minimum level to initiate damage, Int. J. Refract. Met. Hard Mater. 28 (2010) 124–132.
[20] S. Krämer, J. Yang, C.G. Levi, Infiltration-inhibiting reaction of gadolinium zirconate thermal barrier coatings with CMAS melts[J], J. Am. Ceram. Soc. 91 (2) (2008) 576–583.
[21] L. Li, N. Hitchman, J. Knapp, Failure of thermal barrier coatings subjected to CMAS attack, J. Therm. Spray Technol. 19 (1–2) (2009) 148–155.
[22] P. Mohan, B. Yuan, T. Patterson, T. Patterson, V. Desai, Y. Sohn, Degradation of yttria stabilized zirconia thermal barrier coatings by molten CMAS (CaO-MgO-Al_2O_3-SiO_2) deposits[C] materials science forum, Trans. Tech. Publ. 595 (2008) 207–212.
[23] X. Zhou, B. Zou, L. He, Z. Xu, J. Xu, R. Mu, X. Cao, Hot corrosion behaviour of $La_2(Zr_{0.7}Ce_{0.3})_2O_7$ thermal barrier coating ceramics exposed to molten calcium magnesium aluminosilicate at different temperatures[J], Corros. Sci. 100 (2015) 566–578.
[24] K.M. Grant, S. Krämer, J.P.A. Löfvander, C.G. Levi, CMAS degradation of environmental barrier coatings[J], Surf. Coat. Technol. 202 (4) (2007) 653–657.
[25] P. Mechnich, W. Braue, U. Schulz, High-temperature corrosion of EB-PVD yttria partially stabilized zirconia thermal barrier coatings with an artificial volcanic ash overlay [J], J. Am. Ceram. Soc. 94 (3) (2011) 925–931.
[26] J.M. Drexler, A.L. Ortiz, N.P. Padture, Composition effects of thermal barrier coating ceramics on their interaction with molten Ca–Mg–Al–silicate (CMAS) glass[J], Acta Mater. 60 (15) (2012) 5437–5447.
[27] A.R. Krause, X. Li, N.P. Padture, Interaction between ceramic powder and molten calcia-magnesia-alumino-silicate (CMAS) glass, and its implication on CMAS-resistant thermal barrier coatings[J], Scr. Mater. 112 (2016) 118–122.
[28] P. Poza, J.G. García, C.J. Múnez, TEM analysis of the microstructure of thermal barrier coatings after isothermal oxidation[J], Acta Mater. 60 (20) (2012) 7197–7206.
[29] J.C. Rao, Y. Zhou, D.X. Li, $L1_2$- and $L1_0$-like cation-ordered structures in ZrO_2-Y_2O_3 ceramics, J. Mater. Res. 16 (6) (2001) 1806–1813.
[30] Y.G. Wang, C.Y. Cai, L. Li, L. Yang, Y.C. Zhou, G.W. Zhou, Oxygen vacancy ordering induced displacements of cations in yttria-stabilized zirconia, AIP Adv. 6 (9) (2016) 1–8, 095113.